Preprint Title	Revealing the local crystallinity of single silicon core-shell nanowires using tip-enhanced Raman spectroscopy
Authors	Marius van den Berg, Ardeshir Moeinian, Arne Kobald, Yu-Ting Chen, Anke Horneber, Steffen Strehle, Alfred J. Meixner and Dai Zhang
Publication Date	06 Apr 2020
Article Type	Full Research Paper
ORCID® iDs	Steffen Strehle - https://orcid.org/0000-0002-1261-2894; Dai Zhang - https://orcid.org/0000-0001-8190-3030

Revealing the local crystallinity of single silicon core-shell nanowires using tip-enhanced Raman spectroscopy

Marius van den Berg[1,2], Ardeshir Moeinian[3], Arne Kobald[1,2], Yu-Ting Chen[1,2], Anke Horneber[1,2], Steffen Strehle[4*], Alfred J. Meixner[1,2*], Dai Zhang[1,2*]

Address:

[1]Institute of Physical and Theoretical Chemistry, Eberhard Karls University of Tübingen, Auf der Morgenstelle 15, Tübingen, Germany

[2]Center for Light-Matter Interaction, Sensors & Analytics (LISA+), Eberhard Karls University of Tübingen, Auf der Morgenstelle 15, Tübingen, Germany

[3]Institute of Electronic Devices and Circuits, Ulm University, Albert-Einstein-Allee 45, Ulm, Germany

[4]Institute of Micro- and Nanotechnology, Technische Universität Ilmenau, Max-Planck-Ring 12, Ilmenau, Germany

Email: Dai Zhang, dai.zhang@uni-tuebingen.de;

Alfred Meixner, Alfred.meixner@uni-tuebingen.de

Steffen Strehle, steffen.strehle@tu-ilmenau.de

* Corresponding authors

Abstract

Tip-enhanced Raman spectroscopy is combined with polarization angle-resolved spectroscopy to investigate the nanometre-scale structural properties of core-shell silicon nanowires (crystalline Si core and amorphous Si shell), which were

synthesized by platinum-catalyzed vapor-liquid-solid growth and silicon overcoating by thermal chemical vapour deposition. Local changes in the fraction of crystallinity are characterized for those silicon nanowires at an optical resolution of about 300 nm. Furthermore, we are able to resolve the variations in the intensity ratios between the crystalline Si and the amorphous Si Raman peaks by applying tip-enhanced Raman spectroscopy, at sample positions being eight nanometers apart. The local crystallinity revealed using confocal Raman spectroscopy and tip-enhanced Raman spectroscopy agree well with the high-resolution transmission electron microscopy measurements. Additionally, the polarizations of Raman scattering and the photoluminescence signal from the tip-sample nanogap are explored by combining polarization angle-resolved emission spectroscopy with tip-enhanced optical spectroscopy. Our work demonstrates the significant potential of resolving local structural properties of Si nanomaterials at the sub-10 nanometer scale using tip-enhanced Raman techniques.

Keywords

Tip-enhanced Raman spectroscopy, core-shell nanowire, silicon, polarization angle-resolved spectroscopy, local crystallinity

Introduction

The properties of silicon are long standing topics of various investigations because silicon is still the most widely used semiconductor material for a broad range of micro- and nano-electromechanical systems, microelectronics, and photovoltaics [1, 2]. Nanostructured silicon, such as bottom-up grown nanowires [3], were also synthesized serving as multifunctional platforms for field-effect transistors [4-6],

photovoltaic devices [7-10] and miniaturized chemical sensors [5, 11, 12]. A key element for many of those devices are high-quality nanoscale semiconductor junctions, such as pn-junctions that ensure the intended electronic functionality of such nanoscale building blocks. A rational and well-established synthesis strategy for the creation of complex silicon nanostructures is metal-catalyzed vapor-liquid-solid (VLS) nanowire growth [13]. VLS nanowire growth belongs to the gas-phase synthesis procedures, similar to chemical vapor deposition (CVD), and enables direct nanowire growth in a bottom-up manner. The nanowire composition, such a doping concentration, can be controlled by adequate adjustment of the synthesis gas mixture, e.g. by setting the SiH_4/B_2H_6 ratio in case of boron-doped silicon nanowire synthesis. A rational strategy to obtain radial homo- and heterojunctions is to overcoat the as-grown nanowires within the same reaction chamber by implementing a conventional CVD process (e.g. thermal SiH_4-CVD) yielding core-shell nanowires [14]. Although ideal epitaxial growth is frequently assumed, the crystallinity of the shell is intimately linked to multiple process parameters and thus, subject to local variations at the nanoscale [15]. Control and knowledge of the crystal state of core-shell-nanowires is important to rationally design, understand and control the optical and electronic behavior of nanowire building blocks. Hence, there is an inherent need for non-destructive characterization techniques that are able to elucidate the local crystallinity.

Raman spectroscopy is such a type of non-destructive characterization technique, which has become the preferred method to investigate structural properties of silicon samples [16, 17]. Mizoguchi et al. and Hopkins et al. utilized it to show the influence of stress on the crystal lattice orientation angles and to determine the degree of surface roughness. Kolb et al. measured the lattice orientational change due to the laser induced temperature variation [18]. Furthermore, crystalline (*c*-Si) and

amorphous (*a*-Si) Si show different Raman peaks, which can be used to determine the fraction of crystallinity and bond-angle distortion.[19, 20] For example, Nikolenko et al.[21] investigated the local structure and phases of silicon by measuring its Raman peaks along a silicon wire prepared under high pressure. They found a shift of the transverse optical (TO) phonon peak across the wire, which could be attributed to a non-uniform growth of the nanowire and different crystalline phases. Agbo et. al. showed in the meantime that polarized excitation Raman spectroscopy is useful to distinguish hydrogenated nano-crystalline silicon films (*nc*-Si) from *a*-Si and *c*-Si areas [22].

Although, Raman spectroscopy is an overall powerful tool to characterize the material properties of Si, this technique requires still an improvement regarding the sensitivity and the diffraction-limited optical resolution. Thus, a high-resolution technique that reveals both, the structural and the optical properties at nanometer scale is needed to study the fraction of crystallinity and defects within the silicon nanowires (SiNWs). Tip-enhanced Raman spectroscopy (TERS) has distinguished itself as a powerful characterization technique, which allows to obtain both, the morphology and the so-called chemical 'finger-print' information simultaneously with a resolution of a few nanometers. The key element of this technique is a sharp tip resembling a nanoscale antenna. This nanoantenna is typically made by chemical-etching of a thin Ag- or Au-wire or by evaporating a Ag or Au thin film on AFM tips. The tip works like an optical antenna when it is brought as close as a few nanometers to the sample surface and, when it is illuminated with a tightly focused laser beam. The near-field localized at the tip apex enhances the optical field in the tip-sample gap by several orders of magnitude and simultaneously directs the emitted photons from the gap into the far field for detection. With recent demonstrations of spatial resolution even at Angstrom level [23], TERS has made real chemical nanospectroscopy possible [24-26].

In this work, the structural properties of VLS-grown core-shell silicon nanowires are investigated using both confocal Raman spectroscopy and TERS. Notably, the silicon core is single-crystalline while the shell should be amorphous to nanoscrystalline based on the synthesis process parameters. Hence, these nanowires resemble ideal objects to study local crystallinity variations at the sub-ten nanometer scale using TERS. Furthermore, polarization angle-resolved spectroscopy is for the first time combined with TERS, in order to reveal the different polarizations of Raman scattering and the photoluminescence from the tip-sample nanogap.

Results and Discussion

Silicon nanowire core-shell morphology

In accordance with the VLS synthesis method (see **Experimental**), the utilized Pt catalyst or finally Pt_xSi_x remains at the tip of the nanowire during growth. However, it is worth mentioning that other growth mechanisms of Pt catalyzed nanowires were also previously observed [27]. The overall morphology of Pt catalysed silicon nanowires was investigated by transmission electron microscopy (TEM). High-resolution TEM investigation of the core area of the Pt catalyzed SiNWs indicates that Pt-catalyzed SiNWs are mainly single-crystalline. However, in some areas along the nanowire axis defects can be as well present (Figure 1 a). The diffraction pattern of this part of the SiNW (Figure 1 b) shows more than one reflection, which indicates that the structure of the SiNW consists presumably of segments or grains with different orientation. Furthermore, catalyst migration along the SiNW backbone was observed in some cases (Figure 1 c). Although SiNW growth by the VLS mechanism possess a crystalline morphology, silicon shells deposited onto nanowires by thermal CVD (here using a temperature of 520 °C) can be amorphous [15]. Figure 1 d) illustrates in this regard a core-shell SiNW with a distinct contrast in core/shell

morphology. As it can be seen in insets e) and f), the core region of the nanowire appears single-crystalline and the crystal planes end abruptly at the core-shell interface. The shell region of the nanowire exhibits an amorphous morphology.

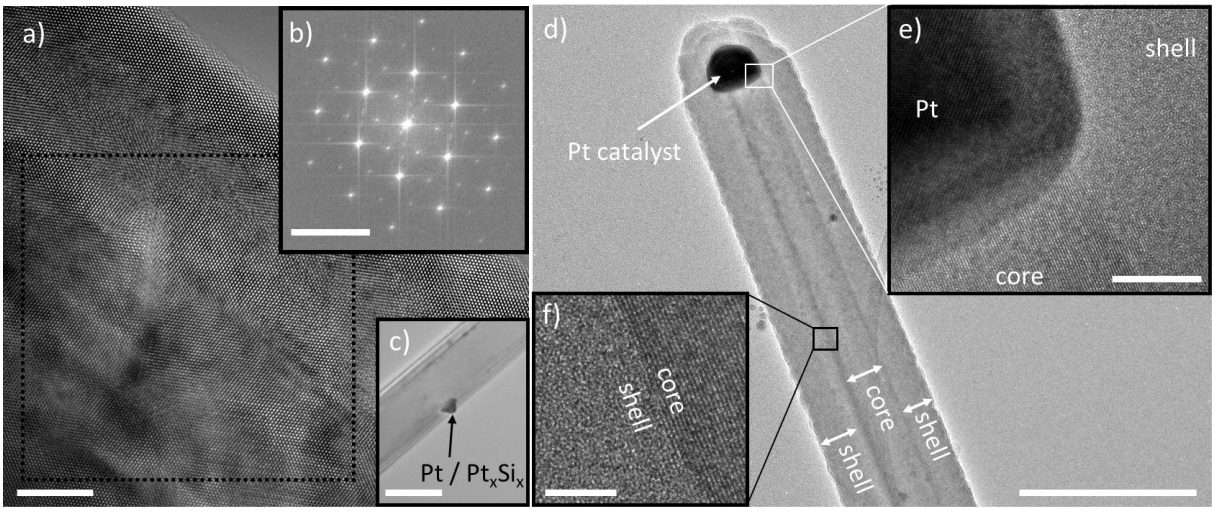

Figure 1 a) High-resolution TEM image of a Pt-catalyzed SINW segment that exhibits several defects and differently oriented crystalline grains. b) The fast Fourier transformation image of the indicated area in a). c) TEM image showing a migrated metal particle on a SiNW. d) TEM image of a Pt catalyzed core-shell SiNW showing the morphology of the junction between SiNW core. e) Pt-silicide catalyst and the shell region; f) illustration of the interface between the SiNW core and the shell. Scale bars are for a) 5 nm, b) 5 nm^{-1}, c) 100 nm, d) 200 nm, e) 10 nm and f) 5 nm.

Confocal optical microscopy of silicon nanowires

As the first step, core-shell SiNW grown from a platinum catalyst [27] are characterized using a home-built confocal optical microscope. Figure 2 a) shows the representative geometry of these SiNWs, which are characterized using a helium ion microscope. In Figure 2 b) a hyper-spectral image composed of 32 x 24 spectra taken from an area of 20 x 20 µm is shown, where bundles of SiNWs can be seen. In Figure 2 c) two spectra taken from the positions marked with orange and blue points are illustrated. The light blue and orange lines show the raw spectra, which are composed of a broad photoluminescence continuum emitted from the underlying Au thin film and sharp Raman peaks. For the further analysis, these spectral features are fitted using Lorentzian functions for the Raman peaks and a Gaussian function for

the photoluminescence peak. The first order transverse optical mode of *c*-Si (F_{2g}) leads to a sharp Raman peak at 520 cm^{-1}; whilst *a*-Si is detected by a broad band centered at 495 cm^{-1} [28]. A thin oxide layer that covers SiNWs, causes a broad Raman peak at 480 cm^{-1} and significantly influences the shape of the F_{2g} peak leading to a broadening and a stronger baseline of this peak [28, 29]. In order to quantitatively evaluate the local structural composition, the respective *a*-Si and *c*-Si Raman peak intensities are therefore determined by integrating the total Raman

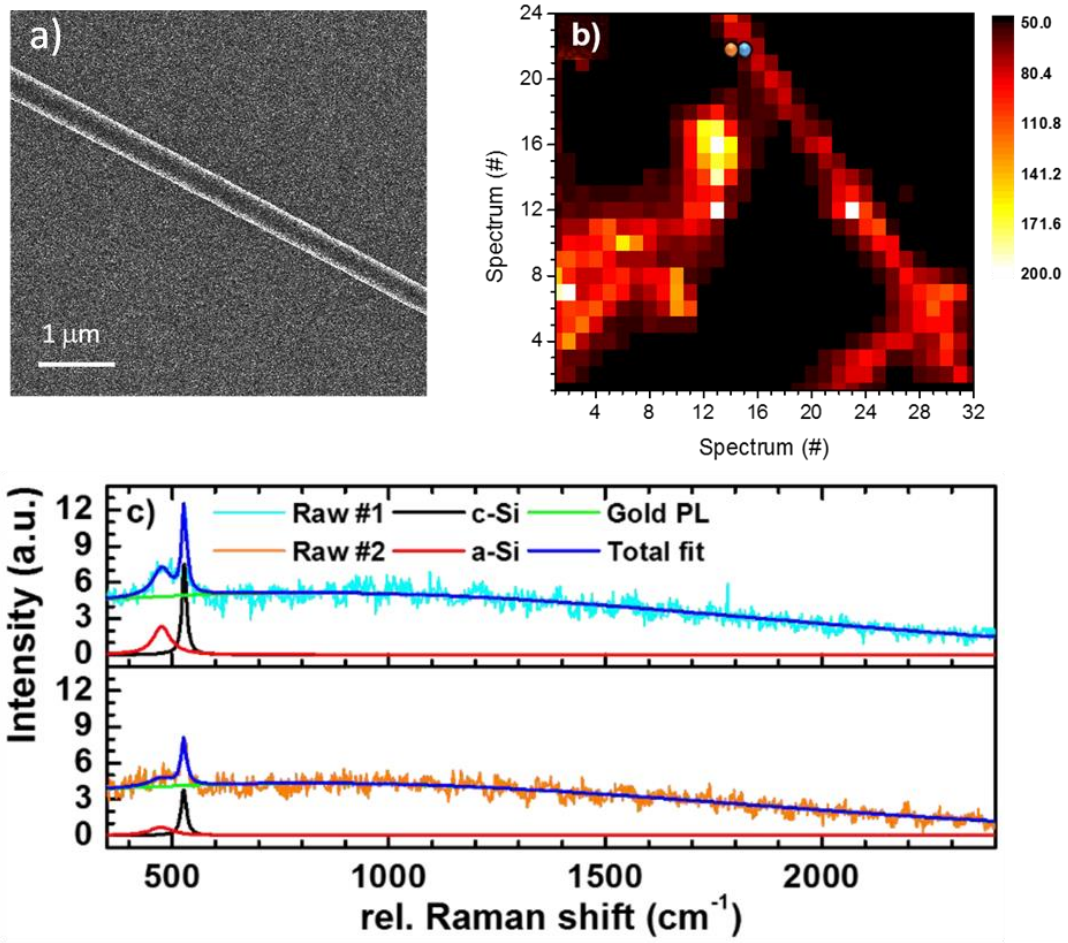

Figure 2 a) Representative helium ion microscope image of a SiNW that is supported on an Au film-coated Si wafer. b) Hyperspectral image of the sample surface. 32 x 24 spectra are taken from a 20 x 20 µm area. The colour scale is based on the integrated intensity of each taken spectrum. c) Two example spectra taken from the marked positions as indicated by the orange and blue dot in b). The original data is plotted in light-blue and orange. The Raman peaks of crystalline and amorphous silicon are fitted using Lorentzian functions, which are indicated as the black and red lines, respectively. The total fit for both spectra is indicated by the dark-blue line. Furthermore, the spectral background is fitted (green line) using a Gaussian function. The background is resulting from photoluminescence of the Au film. Excitation source: 636.3 nm continuous wave diode laser.

intensities from spectral ranges of 460 - 500 cm^{-1} for *a*-Si, and 514 - 532 cm^{-1} for *c*-Si after subtracting the broad PL background. To calculate the crystalline fraction (f_c) we use the model of Smit et al. [30] as shown in equation (1). The areas of the Raman peaks of the *c*-Si and *a*-Si are used as respective intensities ($I_{c\text{-}Si}$ and $I_{a\text{-}Si}$) for the calculation of crystalline fraction (f_c).

$$f_c = I_{c\text{-}Si} / (I_{c\text{-}Si} + 0.8\, I_{a\text{-}Si}) \qquad (1)$$

For the orange and blue marked spots in Figure 2 b), the corresponding two spectra are shown in Figure 2 c). Values of $f_c = 0.45$ and $f_c = 0.57$ are calculated, respectively. A further confirmation of the lower crystallinity in the orange-dot marked spot comes from the full width at the half maximum (FWHM) of the Raman peaks. Both *a*-Si and *c*-Si peaks are significantly broader, 25% and 13% respectively, at the orange spot compared to those from the blue-dot marked position. These results agree well with the morphology revealed in the high resolution TEM images (Figure 1 c) since the orange dot marked sample position locates at the perimeter of the SiNW, where the *a*-Si shell dominates.

In order to achieve a detailed map of the crystalline fraction (f_c) along a single Si NW, 16 x 16 spectra are collected from a 5 x 5 um area that is marked by the yellow frame in Figure 3 a). Each hyperspectral image consists of 16 x 16 spectra, resulting in step size of 312.5 nm with a diffraction limited laser focus of about 300 nm. In Figure 3 b) and c) Raman spectra were taken along the white arrow are shown. In Figure 3 c), the *a*-Si and *c*-Si Raman peaks are acquired with a higher resolving grating with 600 lines/mm in contrast to a 150 lines/mm grating in b). The pink arrow in Figure. 3 c) indicates the spectrum taken close to the ring-shaped pattern within the yellow frame in Figure. 3 a).

It can be clearly seen that the intensity ratios between the *a*-Si and *c*-Si Raman peaks varies along the SiNW, mainly due to the changing in the *c*-Si Raman intensity. To quantify this tendency, the 16 x 16 spectra are processed by peak fitting and integration as described above. The intensity distribution of the *a*-Si Raman peak is plotted in Figure 3 d), which appears to be rather constant along the silicon wire. It agrees with the TEM image in Figure 1 c), where a homogenous presence of the amorphous component in the shell can be seen. On the contrary, the intensity of the *c*-Si peak (Figure 3 e) shows a clear decrease at the lower part of the SiNW. This

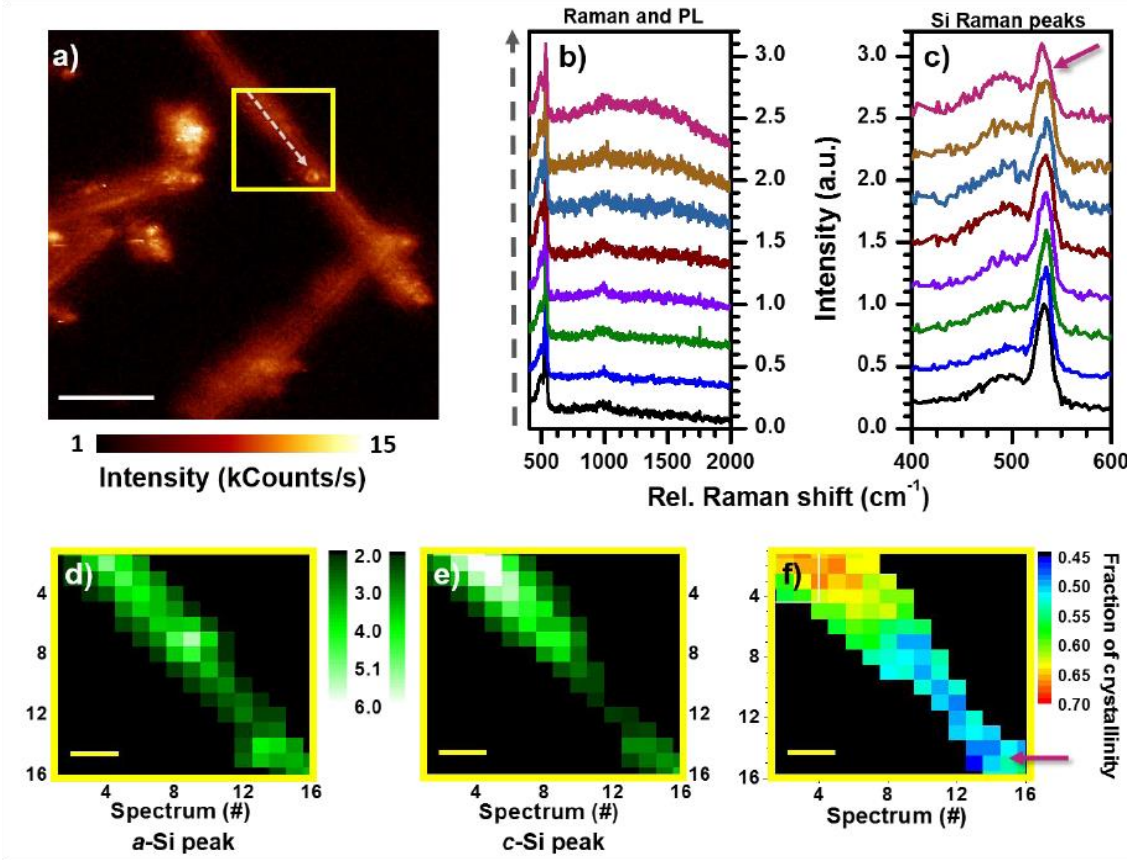

Figure 3 a) A confocal 20 µm x 20 µm image of two intersecting SiNWs on the gold substrate. The yellow square marks the region where a hyperspectral image with16 x 16 points was taken. b) Raman spectra with PL background were collected along the white arrow inside the yellow square in 2 a). c) The evolution in a-Si and c-Si peak intensity along the scan direction showed in a). Spectra are vertically shifted for clarity. The integrated areas of the a-Si peak and the c-Si peak are plotted in d) and e), respectively. The calculated fraction of crystallinity is plotted in f). The drop in the fraction of crystallinity at the right bottom corner, corresponds to the ring-shaped pattern inside the yellow square in a). Its corresponding spectrum and position are indicated with a pink arrow in c) and f) respectively. The white scale bar in a) indicates 5 µm, and yellow scale bars are 1 µm in d), e) and f).

could originate from a defect, visible as the ring-shaped pattern in Figure 3 a), located at the bottom end of the yellow square. This observation is in line with the high-resolution TEM image in Figure 1c), where a migrated metal particle originating from the catalyst is shown. Implementing the intensity information from the Figures 3 d) and e) into equation (1), a map of the crystalline fraction (f_c) along the single SiNW is calculated. As shown in Figure 3 f), the lowest crystalline fraction is about 0.45, and the highest of 0.70. Hence, an overview of the crystallinity property of a single SiNW can be obtained at the diffraction limited optical resolution of about 300 nm.

Tip-enhanced Raman spectroscopy of silicon nanowire

The evolution of *c*-Si and *a*-Si Raman peaks, and therefore the fraction of crystallinity of a single SiNW, is further studied using TERS and the emitted optical signals are analyzed using polarization angle-resolved spectroscopy.

Figure 4 a) shows a SEM image of the tip used for the TERS measurements. Scanning the tip across the laser focus gives an Airy-disc alike pattern (Figure 4 b), which is due to the photoluminescence emitted from the sharp tip apex. Irregularities can arise from the slight asymmetry of the tip apex. Figure 4 c) shows the polarization angle-resolved optical pattern of the photoluminescence of gold tip. We

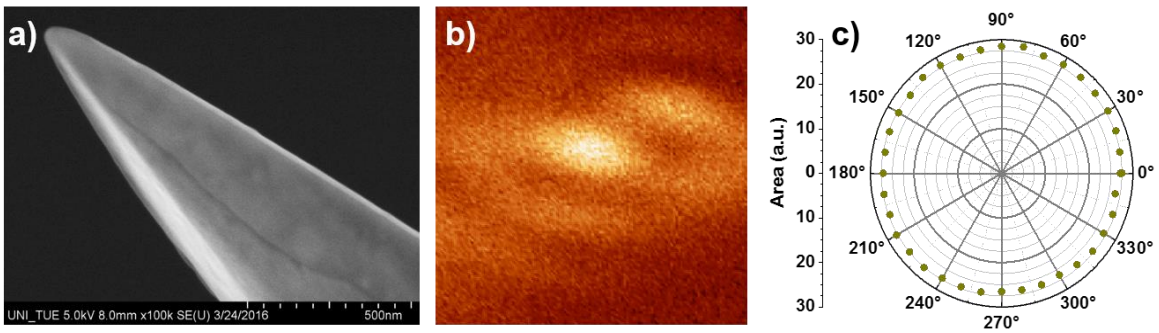

Figure 4 a) Scanning Electron Microscopy (SEM) Image of the tip used, the optical image of the tip in focus is shown in b). The polarization angle resolved luminescence of only the tip in focus without a sample is shown in c). An almost perfectly circular emission pattern is observed.

positioned a Glan-Taylor polarizer in the beam in front of the entrance slit of the spectrometer and collected spectra while rotating the polarizer. The Glan-Taylor prism only transmits the optical signal along its fast axis. Therefore, the angle-resolved polarization of the emitted signal can be obtained by rotating the prism while collecting optical spectra. The circle-shaped pattern is originating from the emission of the plasmonic oscillation along the tip shaft. This is in good agreement with the electric field distribution in the focus of a radially polarized laser beam, where the dominant field component lays out-of-plane (parallel to the tip shaft). Both Figures 4 b) and c) demonstrate that the tip apex can be well-excited, which is a precondition for producing a localized near-field at the tip apex.

Afterwards, we approached the sample to the tip and recorded the topography (size: 250 x 250 nm) along the perimeter of a SiNW. The tip-sample distance is controlled by a shear-force feedback. For this purpose, the tip is mounted on an oscillating tuning fork, which experiences a phase shift of the oscillation upon approach. This phase shift is recorded with a lock-in amplifier and fed to a feedback loop that maintains a constant distance to the sample. The scanned SiNW perimeter is indicated in Figure 5 a). Along the white arrow, there is about 250 nm height-difference from the SiNW to the underlying substrate. A white square shown in the optical image in Figure 5 b) highlights the SiNW measured using the shear-force scanning function of our home-built TERS setup. Eight TERS spectra with a distance of 8 nm, shown in Figure 5 c) were taken along the white arrow in Figure 5 a). The spectra were acquired from bottom to top, with the black spectrum on the SiNW and the yellow-green one on the underlying substrate. Notably, though a clear decrease in *c*-Si intensity is observed across the perimeter of the SiNW, the *a*-Si Raman peak intensity stays nearly constant and indicates the crystal state of SiNW shell. This correlates with a decrease in the fraction of crystallinity from the center to the

perimeter of the SiNW, which can be resolved with the optical resolution of 8 nm. These observations agree well with the morphology revealed by high-resolution TEM images in Figure 1 c).

As a reference measurement, an equal number of far-field spectra (normal Raman spectra) are taken from the same sample positions (Figure 5 d), which show no differences in the intensity ratio between the *a*-Si and *c*-Si Raman peaks from neighboring data points. Furthermore, even between the SiNW and the underlying substrate, no decrease in the *c*-Si Raman peak that can be seen. Additionally, the intensity ratios between the *a*-Si and *c*-Si Raman peaks are nearly constant in this case. This can be explained by the excitation area by the confocal laser focus, which is at least an order of magnitude bigger than that in TERS experiment. Therefore, only a marginal difference between two spectra of 8 nm apart is visible, even when

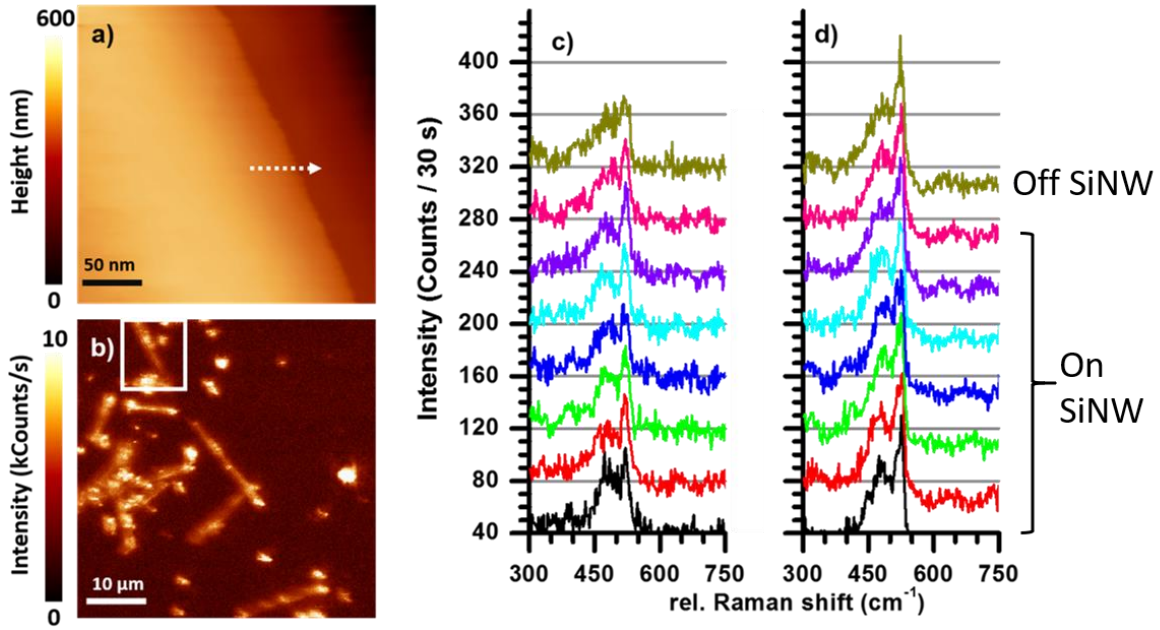

Figure 5 a) A shear-force SPM 250 nm x 250 nm topography image of a silicon wire edge. The white arrow indicates the range and direction along which the Raman spectra in c) and d) are collected. b) Location of the wire indicated on the 50 x 50 µm optical image by a white square. TERS spectra with 8 nm between them are shown in c) and are vertically offset for clarity. A decreasing c-Si peak can be seeing when moving away from the edge across the arrow. Confocal spectra taken at exactly the same spots as the TERS spectra are shown in d), where the intensity ratios between the c-Si and a-Si shows nearly no variations. Both TERS and confocal spectra have been acquired with 170 µW excitation power, and an integration time of 30 seconds per spectrum.

the sampling point is not on the Si NW anymore (the 'off SiNW' spectrum, Figure 5 d). Beeman et al.[20] suggested to use the root mean square bond-angle distortion $\Delta\Theta$ to evaluate the crystalline and amorphous Si, which can be calculated using the full width half maximum (FWHM, in cm^{-1}) of the one-phonon Raman peak of Si at about 520 cm^{-1} with the equation:

$$FWHM = (15 + 6\,\Delta\Theta)/2 \qquad (2).$$

In *c*-Si with a diamond cubic structure, $\Delta\Theta$ has a value of $0°$, whereas in *a*-Si films $\Delta\Theta$ was experimentally determined to be in the range of $7.7° \leq \Delta\Theta \leq 10.5°$. In our experiments we calculated $\Delta\Theta_{avg,n\text{-}f} = 9.2°$ and $\Delta\Theta_{avg,conf} = 8.3°$ based on the near-field and confocal spectra, respectively. The slightly higher value of $\Delta\Theta$ determined through TERS could be due to the nanometer-sized penetration depth of the near-field excited at the tip-apex as compared to the far-field laser focus. Since the SiNW is containing a *c*-Si core and an *a*-Si shell as shown in the TEM images (Figure 1), the shell could be better excited by the evanescent electromagnetic near-field at the tip-apex.

The highly improved optical resolution achieved TERS depends strongly on the tip-sample interaction. When the sample is positioned within close proximity of the excited tip apex, the substrate material gains influence via the coupling between the oscillation field in the excited tip and its mirror image in the substrate. We have shown from previous theoretical work that the permittivity of the tip and the substrate influences the near-field enhancement at the tip apex significantly [31]. In the next set of experiments, we combined angle-resolved polarization measurements with TERS to investigate the effects of tip-sample interactions on the optical signals. In Figure 6 a) the topography of a SiNW surface is shown. Along the dashed arrow, 32 spectra are collected, and eight of them are plotted in Figure 6 b). Although all the spectra are taken on the surface of one SiNW, intensity ratio differences between the *c*-Si

and *a*-Si Raman peaks are visible, which can be attributed to the variations of the local crystallinity within one SiNW. Furthermore, polarization angle-resolved emission measurements are performed at two adjacent positions that is 30 nm apart, marked by the blue and purple points in Figure 6 a). The integrated area of the *c*-Si Raman peak is plotted against the rotation angle of the fast axis of the Glan-Taylor polarizer. The measured polarization angle-resolved emission patterns are rather similar from the two sample positions, indicating similar polarization states of the Raman scatterings from there. Interestingly, when plotting the photoluminescence signal

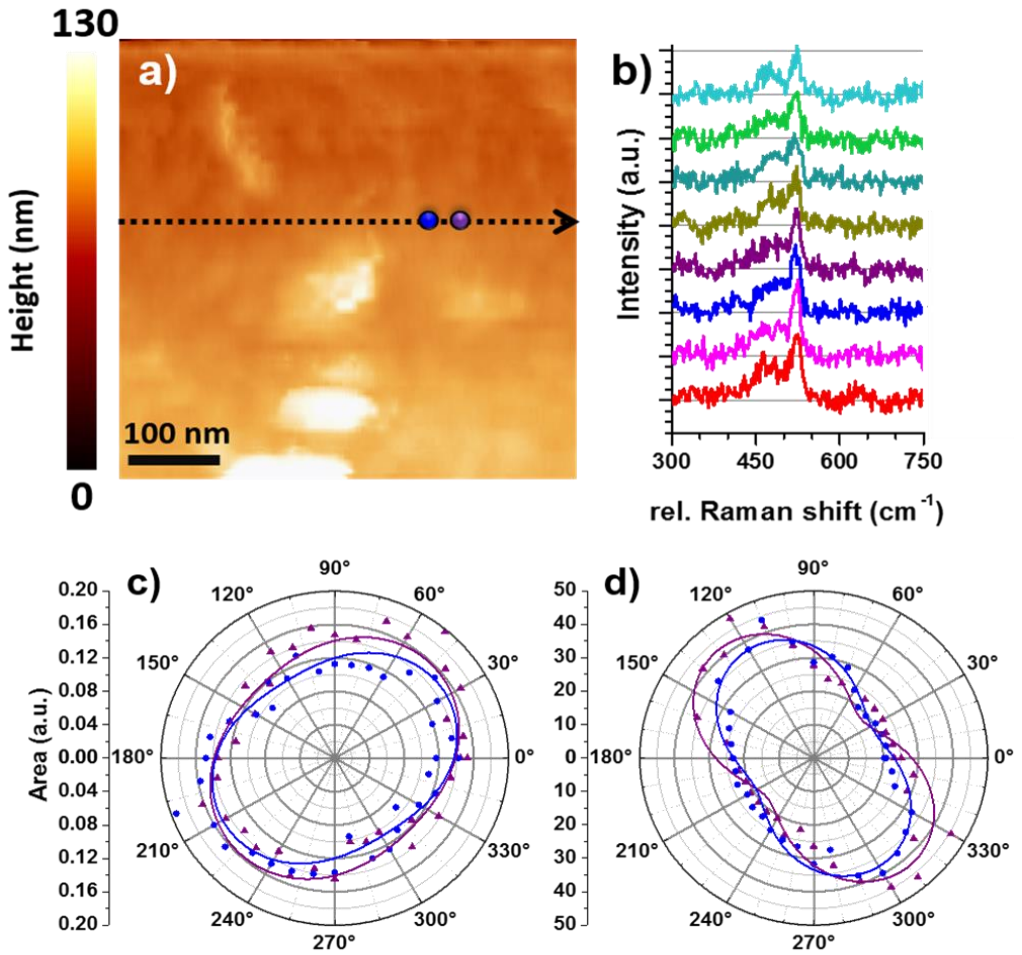

Figure 6 a) Topographical image on top of a SiNW. The dashed arrow shows the region where the 32 Raman spectra are taken. The blue and purple dots indicate the positions where the polarization angle-resolved measurements where performed. b) Eight of the collected Raman spectra along the white arrow in a) are plotted, showing varying c-Si Raman peak intensities. c) Polarization angle-resolved Raman scattering of the c-Si Raman peak against the rotation angle of the Glan-Taylor polarizer. The triangles and circles are the original data, whilst the close lines are to guide the eyes. d) Polarization angle-resolved photoluminescence patterns collected from the same sample positions, indicated in a).

against the rotation angle of the Glan-Taylor polarizer, as shown in Figure 6 d), the patterns are distinctly different from those in Figure 6 c). Note that the Raman intensity and the photoluminescence intensity used for the plotting Figure 6 c) and d) are derived from the same spectrum. Therefore, potential artefacts induced by any instrument operation errors can be excluded. Furthermore, upon approaching the gold tip to the SiNW, the angle-resolved polarization pattern changes from the circle-shaped pattern (Figure 4 c) to a more-structured shape in Figure 6 d). It is likely that the high refractive index of SiNW has a certain impact on the polarization of the photoluminescence emitted from the narrow gap between the gold tip and the Si NW. A more quantitative investigation of the polarization angle-resolved emission patterns in Figure 6) will be further pursued. The results shown in Figure 4) and Figure 6) demonstrate that it is possible to combine the polarization angle-resolved experiments with the TERS setup, which has been rarely pursued so far in the state-of-the-art. The successful combination of both techniques is promising for developing new strategies to resolve the structural properties at the sub-10 nanometer scale, based on the polarization properties of Raman scatterings, demonstrated here for *c*-Si and *a*-Si using a core-shell SiNW.

Conclusion

Local structural properties, like changes in the fraction of crystallinity of a *c*-Si core and *a*-Si shell silicon nanowire are characterized confocally at an optical resolution of about 300 nm. Applying tip-enhanced Raman spectroscopy, we show that variations of the intensity ratio between the crystalline Si and amorphous Si Raman peaks at sample positions as close as eight nanometers can be revealed. Furthermore, the polarizations of Raman scattering and photoluminescence signals locally emitted

from a single SiNW are explored by combining polarization angle-resolved emission spectroscopy with tip-enhanced optical spectroscopy. Our work demonstrates the high potential of resolving local structural properties of nanomaterials, here demonstrated for silicon, at the sub-10 nanometer scale using tip-enhanced Raman techniques. TEM investigations are in line with TERS results, which supports the idea that TERS can be used as a micro/nano-structure characterization technique.

Experimental

Core-shell silicon nanowires are synthesized in two steps. At first, SiNWs were grown by utilizing the VLS growth mechanism [13] using dewetted Pt thin films as the growth catalyst [27] at a growth temperature of 720 °C, which yields a certain SiNW diameter distribution. VLS nanowire growth is carried out in a quartz tube furnace with precursor gas mixture of H_2 (270 sccm) and of SiH_4 (30 sccm), at a pressure of 100 mbar. Silicon shell growth is done at a temperature of 520 °C with a gas mixture of H_2 (10 sccm) and of SiH_4 (100 sccm), at a pressure of 100 mbar. The silicon shell growth rate is under these conditions in the range of 1 nm/min and yields a thickness of approximately 25 nm. To make confocal Raman and TERS investigations of individual nanowires, SiNWs are released from their original growth substrate by ultra-sonicating the growth substrate in purified water. For Raman and TERS investigations, nanowires are deposited on gold coated silicon wafers as carrier substrates. For transmission electron microscopy (TEM), nanowires are deposited on copper TEM grids with lacey-carbon nets.

Using a home built parabolic mirror (NA: 0.998) [32] assisted setup, we achieve a diffraction-limited confocal resolution by illumination with a radially polarized laser beam [33]. With a 636.3 nm diode laser operating in continuous wave mode we

obtain a focus diameter of roughly ~300 nm [34]. To further increase the resolution a chemically etched gold tip, attached to a tuning fork, is brought into the focus. A plasmonic oscillation is generated with a radially polarized laser beam along the tip-axis. Here the local field intensity is greatly increased leading to a strong local near-field confined at the tip apex. This gives rise to the capability of tip enhanced Raman spectroscopy (TERS). TERS combined with the scanning probe microscopy (SPM) greatly improves the spatial and optical resolution down to the nanometer scale when the sample and tip are both simultaneously in the optical focus [35-39]. It also allows for the collection of the correlated topography and optical images [40, 41]. For polarization angle-resolved emission measurements, a Glan-Taylor prism as polarization filter is positioned in front of the entrance slit of the spectrometer.

Acknowledgements

We thank D. Geiger (Ulm University) for the high-resolution TEM of the SiNWs, M. Turad and C. Dobler for characterizing the SiNWs using helium-ion microscope and E. Nadler for characterizing the Au tip using scanning electron microscopy. We also thank the program WSXM, which is used for illustrating the optical and topography images [42].

References

1. Tallur, S.; Bhave, S. A. *Nano letters* **2013**, *13* (6), 2760-2765.
2. Dallas, W.; Polupan, O.; Ostapenko, S. *Measurement Science and Technology* **2007**, *18* (3), 852.
3. Schmidt, V.; Wittemann, J. V.; Senz, S.; Gösele, U. *Advanced Materials* **2009**, *21* (25‐26), 2681-2702.
4. Guerfi, Y.; Larrieu, G. *Nanoscale research letters* **2016**, *11* (1), 1-7.
5. Zulfiqar, A.; Patou, F.; Pfreundt, A.; Papakonstantinopoulos, C.; Svendsen, W. E.; Dimaki, M. *Sensing and Bio-Sensing Research* **2017**, *13*, 88-95.
6. Chen, K.-I.; Li, B.-R.; Chen, Y.-T. *Nano today* **2011**, *6* (2), 131-154.

7. Garnett, E.; Yang, P. *Nano letters* **2010**, *10* (3), 1082-1087.
8. Tsakalakos, L.; Balch, J.; Fronheiser, J.; Korevaar, B.; Sulima, O.; Rand, J. *Applied Physics Letters* **2007**, *91* (23), 233117.
9. Stelzner, T.; Pietsch, M.; Andrä, G.; Falk, F.; Ose, E.; Christiansen, S. *Nanotechnology* **2008**, *19* (29), 295203.
10. Adachi, M.; Anantram, M.; Karim, K. *Scientific reports* **2013**, *3* (1), 1-6.
11. Crescentini, M.; Rossi, M.; Ashburn, P.; Lombardini, M.; Sangiorgi, E.; Morgan, H.; Tartagni, M. *Biosensors* **2016**, *6* (2), 15.
12. Cao, A.; Sudhölter, E. J.; De Smet, L. C. *Sensors* **2014**, *14* (1), 245-271.
13. Wagner, R.; Ellis, W. *Applied physics letters* **1964**, *4* (5), 89-90.
14. Lauhon, L. J.; Gudiksen, M. S.; Wang, D.; Lieber, C. M. *Nature* **2002**, *420* (6911), 57-61.
15. Moeinian, A.; Hibst, N.; Geiger, D.; Biskupek, J.; Strehle, S. *IEEE Transactions on Nanotechnology* **2017**, *16* (5), 736-740.
16. Piscanec, S.; Cantoro, M.; Ferrari, A.; Zapien, J.; Lifshitz, Y.; Lee, S.; Hofmann, S.; Robertson, J. *Physical Review B* **2003**, *68* (24), 241312.
17. De Wolf, I.; Maes, H.; Jones, S. K. *Journal of Applied Physics* **1996**, *79* (9), 7148-7156.
18. Mizoguchi, K.; Nakashima, S. i. *Journal of applied physics* **1989**, *65* (7), 2583-2590.
19. Voutsas, A.; Hatalis, M.; Boyce, J.; Chiang, A. *Journal of Applied Physics* **1995**, *78* (12), 6999-7006.
20. Beeman, D.; Tsu, R.; Thorpe, M. *Physical Review B* **1985**, *32* (2), 874.
21. Nikolenko, A.; Strelchuk, V.; Klimovskaya, A.; Lytvyn, P.; Valakh, M.; Pedchenko, Y.; Voroschenko, A.; Hourlier, D. *physica status solidi c* **2011**, *8* (3), 1012-1016.
22. Agbo, S.; Sutta, P. *Digest Journal of Nanomaterials & Biostructures (DJNB)* **2013**, *8* (4).
23. Zrimsek, A. B.; Chiang, N.; Mattei, M.; Zaleski, S.; McAnally, M. O.; Chapman, C. T.; Henry, A.-I.; Schatz, G. C.; Van Duyne, R. P. *Chemical reviews* **2017**, *117* (11), 7583-7613.
24. Huang, T.-X.; Cong, X.; Wu, S.-S.; Lin, K.-Q.; Yao, X.; He, Y.-H.; Wu, J.-B.; Bao, Y.-F.; Huang, S.-C.; Wang, X. *Nature Communications* **2019**, *10* (1), 1-8.
25. Zhang, Y.; Yang, B.; Ghafoor, A.; Zhang, Y.; Zhang, Y.-F.; Wang, R.-P.; Yang, J.-L.; Luo, Y.; Dong, Z.-C.; Hou, J. G. *arXiv preprint arXiv:1908.08720* **2019**.
26. Lee, J.; Crampton, K. T.; Tallarida, N.; Apkarian, V. A. *Nature* **2019**, *568* (7750), 78-82.
27. Hibst, N.; Knittel, P.; Biskupek, J.; Kranz, C.; Mizaikoff, B.; Strehle, S. *Semiconductor Science and Technology* **2015**, *31* (2), 025005.
28. Qi, J.; White, J. M.; Belcher, A. M.; Masumoto, Y. *Chemical physics letters* **2003**, *372* (5-6), 763-766.
29. Wang, R.-p.; Zhou, G.-w.; Liu, Y.-l.; Pan, S.-h.; Zhang, H.-z.; Yu, D.-p.; Zhang, Z. *Physical Review B* **2000**, *61* (24), 16827.
30. Smit, C.; Van Swaaij, R.; Donker, H.; Petit, A.; Kessels, W.; Van de Sanden, M. *Journal of applied physics* **2003**, *94* (5), 3582-3588.
31. Mihaljevic, J.; Hafner, C.; Meixner, A. J. *Optics express* **2013**, *21* (22), 25926-25943.
32. Lieb, M. A.; Meixner, A. J. *Optics express* **2001**, *8* (7), 458-474.
33. Fulmes, J.; Gollmer, D.; Jäger, S.; Schäfer, C.; Horrer, A.; Zhang, D.; Adam, P.-M.; Meixner, A.; Kern, D.; Fleischer, M. *Optics express* **2018**, *26* (12), 14982-14998.

34. Stadler, J.; Stanciu, C.; Stupperich, C.; Meixner, A. *Optics letters* **2008**, *33* (7), 681-683.
35. Zhang, D.; Wang, X.; Braun, K.; Egelhaaf, H. J.; Fleischer, M.; Hennemann, L.; Hintz, H.; Stanciu, C.; Brabec, C. J.; Kern, D. P. *Journal of Raman Spectroscopy: An International Journal for Original Work in all Aspects of Raman Spectroscopy, Including Higher Order Processes, and also Brillouin and Rayleigh Scattering* **2009**, *40* (10), 1371-1376.
36. Tang, X.; van den Berg, M.; Gu, E.; Horneber, A.; Matt, G. J.; Osvet, A.; Meixner, A. J.; Zhang, D.; Brabec, C. J. *Nano letters* **2018**, *18* (3), 2172-2178.
37. van den Berg, M.; Back, J.; Horneber, A.; Meixner, M.; Swider, K.; Ludwigs, S.; Zhang, D. *Macromolecules* **2016**, *49* (21), 8219-8227.
38. Wang, X.; Broch, K.; Schreiber, F.; Meixner, A. J.; Zhang, D. *Physical Chemistry Chemical Physics* **2016**, *18* (23), 15919-15926.
39. Wang, X.; Braun, K.; Zhang, D.; Peisert, H.; Adler, H.; Chassé, T.; Meixner, A. J. *ACS nano* **2015**, *9* (8), 8176-8183.
40. Wang, X.; Broch, K.; Scholz, R.; Schreiber, F.; Meixner, A. J.; Zhang, D. *The journal of physical chemistry letters* **2014**, *5* (7), 1048-1054.
41. Chen, Y.-T.; Pan, L.; Horneber, A.; van den Berg, M.; Miao, P.; Xu, P.; Adam, P.-M.; Meixner, A. J.; Zhang, D. *Nanophotonics* **2019**, *8* (9), 1533-1546.
42. Horcas, I.; Fernández, R.; Gomez-Rodriguez, J.; Colchero, J.; Gómez-Herrero, J.; Baro, A. *Review of scientific instruments* **2007**, *78* (1), 013705.